UC Davis
UC Davis Previously Published Works

Title

Helium interactions with alumina formed by atomic layer deposition show potential for mitigating problems with excess helium in spent nuclear fuel

Permalink

https://escholarship.org/uc/item/36r360df

Authors

Zhang, Shenli
Yu, Erick
Gates, Sean
et al.

Publication Date

2018-02-01

DOI

10.1016/j.jnucmat.2017.11.029

Peer reviewed

eScholarship.org Powered by the California Digital Library
University of California

Journal of Nuclear Materials 499 (2018) 301–311

Contents lists available at ScienceDirect

Journal of Nuclear Materials

journal homepage: www.elsevier.com/locate/jnucmat

Helium interactions with alumina formed by atomic layer deposition show potential for mitigating problems with excess helium in spent nuclear fuel

Shenli Zhang [a], Erick Yu [a], Sean Gates [b], William Cassata [b], James Makel [c], Andrew M. Thron [a], Christopher Bartel [d], Alan W. Weimer [d], Roland Faller [c], Pieter Stroeve [c], Joseph W. Tringe [b, *]

[a] Department of Materials Science and Engineering, University of California Davis, Davis, CA 95616, USA
[b] Lawrence Livermore National Laboratory, Livermore, CA 94550, USA
[c] Department of Chemical Engineering, University of California Davis, Davis, CA 95616, USA
[d] Department of Chemical and Biological Engineering, University of Colorado, Boulder, CO 80309, USA

GRAPHICAL ABSTRACT

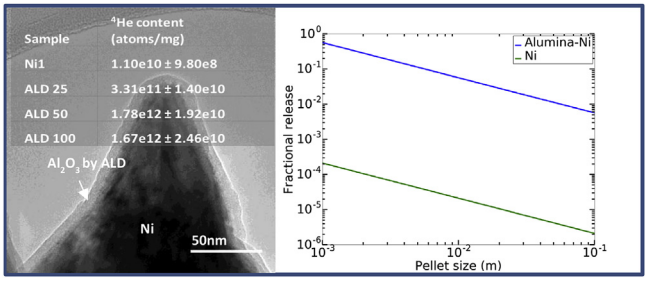

ARTICLE INFO

Article history:
Received 14 July 2017
Received in revised form
25 October 2017
Accepted 18 November 2017
Available online 26 November 2017

Keywords:
Helium
ALD
Alumina
Fuel

ABSTRACT

Helium gas accumulation from alpha decay during extended storage of spent fuel has potential to compromise the structural integrity the fuel. Here we report results obtained with surrogate nickel particles which suggest that alumina formed by atomic layer deposition can serve as a low volume-fraction, uniformly-distributed phase for retention of helium generated in fuel particles such as uranium oxide. Thin alumina layers may also form transport paths for helium in the fuel rod, which would otherwise be impermeable. Micron-scale nickel particles, representative of uranium oxide particles in their low helium solubility and compatibility with the alumina synthesis process, were homogeneously coated with alumina approximately 3–20 nm by particle atomic layer deposition (ALD) using a fluidized bed reactor. Particles were then loaded with helium at 800 °C in a tube furnace. Subsequent helium spectroscopy measurements showed that the alumina phase, or more likely a related nickel/alumina interface structure, retains helium at a density of at least 10^{17} atoms/cm^3. High resolution transmission electron microscopy revealed that the thermal treatment increased the alumina thickness and generated additional porosity. Results from Monte Carlo simulations on amorphous alumina predict the helium retention concentration at room temperature could reach 10^{21} atoms/cm^3 at 400 MPa, a pressure predicted by others to be developed in uranium oxide without an alumina secondary phase. This concentration is sufficient to eliminate bubble formation in the nuclear fuel for long-term storage scenarios, for example. Measurements by others of the diffusion coefficient in polycrystalline alumina indicate values

* Corresponding author.
E-mail address: tringe2@llnl.gov (J.W. Tringe).

https://doi.org/10.1016/j.jnucmat.2017.11.029
0022-3115/© 2017 Elsevier B.V. All rights reserved.

several orders of magnitude higher than in uranium oxide, which then can also allow for helium transport out of the spent fuel.

© 2017 Elsevier B.V. All rights reserved.

1. Introduction

Nuclear reactor fuels are typically dense uranium oxide formed into ~ cm scale pellets and encapsulated in metal for isolation from reactor coolant. Decaying actinides, e.g. short-lived actinides that are produced by capture reactions, as well as n, alpha and n,n + alpha reactions, lead to emission of alpha particles. The volumetric generation of helium from these alpha particles is then a significant concern during long-term spent fuel storage. Actinides actively produce helium during spent fuel storage, such that the increasing helium concentration can plausibly reach its low solubility limit in uranium oxide [1] after more than a hundred years in a repository [2,3]. Due to helium's low diffusion rate below 400 °C [3] under typical repository conditions, helium build-up in grains or at grain boundaries introduces potential for both pellet cracking and fuel embrittlement [3–8]. Although the specific outcome of helium accumulation on the microstructure evolution of reactor fuel is still under study, alleviation of helium buildup can be generally useful for a wide range of spent fuel storage scenarios.

In time, helium migrates along crystallographic grain boundaries over transport distances measured in microns [2]. If the gas could be sequestered in void spaces provided at the time of fuel preparation, or if an alternative diffusion path could be introduced for helium to escape the fuel rod to a controlled collection volume, then in principle the end-of-life pressure could be kept low enough to prevent distortion of the fuel. Previous investigations have focused on improving diffusivity of fission gases in nuclear fuel materials, mainly by doping additives into the uranium oxide matrix [9,10]. In particular, work done by Turnbull and Friskney [11] demonstrated that optimizing diffusion mechanisms along grain boundaries was useful to eliminate gas buildup.

However, there may also be utility in incorporation of a secondary material that has sufficient helium capacity or diffusivity at low pressure, and can be synthesized and optimized independently of fuel chemistry. As an additive in fuel pellet fabrication, it would require only minimal elaboration of the normal process. However, the short helium migration distance in uranium oxide requires very small particles of absorbent mixed very uniformly into the fuel. Coating of the fuel particles themselves would solve this uniformity problem, because the uranium oxide itself is prepared in the form of micron-sized particles prior to consolidation. The actual amount of helium to be transported per particle is small, so only minimal intrinsic absorption in the coating would be required.

A process which seems to offer advantages in this application is atomic layer deposition (ALD) on particles [12]. It is based on reaction of two chemical precursors at the surface of a particulate substrate, and differs from more traditional chemical vapor deposition (CVD) in that the surface is exposed to each precursor separately. The deposition is then self-limiting, enabling precise control of film thickness. After exposure to the first reactant, the surface bears a chemisorbed sub-monolayer; the environment is purged of that reactant, and the second reactant is admitted to form a sub-monolayer of film. This reactant is then purged, and the process repeated, building a conformal coating of as many molecular layers as desired on primary particles. Although ALD is typically used on flat surfaces in the electronics industry, for present purposes a fluidized bed reactor is more appropriate; particles are lifted and agitated by inert carrier gas, so that the bulk properties are those of a fluid. This technique permits excellent control and is scalable to the production rates which would be necessary for nuclear fuel manufacturing.

There are a number of constraints on the chemistry for a coating that facilitates helium transport or capture in nuclear fuel. First, it must be compatible with the nucleonics of the reactor: low neutron absorption and no transmutation into a material which would not sequester helium. Second, the coating must be thermodynamically compatible with the reactor fuel (and to a lesser extent, the cladding alloy) over the expected lifetime of the fuel. Given the high temperature, long time, and small distances involved, even slight chemical reactivity would compromise the function of the coating. The highest temperatures of the nuclear fuel cycle occur during sintering. Sintering temperatures range from 1600 °C to 1800 °C [13–18]. However, a recent study has demonstrated fuel sintering at temperatures as low as 835 °C via spark plasma sintering (SPS) [15]. Lower sintering temperatures open an array of potential materials to be used as fuel additives that could not maintain their favorable properties toward helium sorption upon exposure to temperatures over 1600 °C.

Alumina is an inert metal oxide potentially suitable with CERCER and CERMET nuclear fuels, which are based on ceramic MgO and metal Mo matrices, respectively. The interaction with implanted helium with alumina, MgO, and other inert matrix metal oxides has been examined by van Veen et al. [19] Alumina was chosen for study here because of its compatibility with the promising particle ALD process for distribution of the material around nuclear fuel particles. A comprehensive review of ALD chemistry shows the compatibility of the ALD alumina synthesis process with both uranium oxide and nickel substrates [20]. Alumina has been demonstrated to be thermodynamically compatible with the uranium oxide reactor fuel, i.e., no new phase will form up to 2000 K [21,22]. Also, aluminum's low neutron cross section [23] precludes significant neutron interactions during nuclear fuel operation and storage. In fact, fuels directly incorporating aluminum for, among other advantages, improved thermal conductivity have been previously investigated [24,25]. Helium transport properties in alumina can be understood with complementary data such has been previously obtained by van Veen [19] and Hurst [26]. Finally, there are indications that alumina surrounding nuclear fuel particles can improve mechanical stability of the fuel composites [15]. In the future, ALD processes may be developed for inert metal oxides with greater thermal stability, such as yttria-stabilized zirconia, or metal silicates. This study, however, focuses exclusively on nickel particles as surrogates for uranium oxide nuclear fuel and alumina as a first material for examination to facilitate helium transport and retention.

2. Experimental and simulation methods

2.1. Materials

Nickel particles (diameter ~3 μm, 99.7%, Aldrich Chemical Company) were used as surrogate substrates for uranium, since helium is expected to behave comparably in alumina on both nickel and uranium oxide particles. ALD alumina also shows comparable

affinity for both nickel and uranium oxide surfaces because the ALD reaction processes mainly depend on a hydroxylating substrate surface to proceed [20]. Moreover, nickel has comparably low helium solubility relative to single crystal uranium oxide [27]. We measured the Brunauer- Emmett-Teller (BET) surface area of these nickel particles to be 0.617 ± 0.014 m^2/g, with nitrogen (Micrometrics Gemini V BET Surface Area Analyzer). This is a lower bound for the surface area for helium, due to the smaller physical size of helium atoms compared to nitrogen molecules.

A custom fluidized bed reactor (FBR) [28] was used for the gas-delivery of the reactive ALD precursors ($Al(CH_3)_3$ and H_2O). This chemistry has been used extensively to deposit conformal Al_2O_3 films by ALD [29,30], including on Ni [30]. Here, three sample types were prepared corresponding to 25, 50, and 100 ALD cycles using a deposition temperature of 177 °C and pressures of 1–10 torr.

2.2. Helium spectroscopy

All samples were treated in argon (1 l/m, 800 °C, 18 h) followed by helium (0.5 l/m, 800 °C, 18 h). Copper getters were employed upstream of the nickel particles during the heat treatment to scavenge oxygen and any other trace reactive molecules present in the source gas to prevent reaction of these molecules with the ALD alumina or the nickel. After the completed helium treatment, the portion of the copper getters immediately upstream from the ALD-coated nickel samples appeared pristine (unreacted) by visual inspection, indicating minimal interaction of the particles with species other than noble gases.

Helium measurements were performed in the Livermore Noble Gas Laboratory using a Nu Instruments Noblesse noble gas mass spectrometer. All measurements were performed using a peak hopping routine on a single electron multiplier. Samples for analysis were encapsulated in high-purity platinum-iridium alloy tubes and placed under ultra-high vacuum conditions. The samples were incrementally degassed using a 75 W Photon Machines diode laser ($\lambda = 970$ nm) equipped with a co-axially aligned optical pyrometer for temperature control. As part of our helium spectrometry measurement process, samples are first brought to elevated temperatures (>200 °C) in vacuum, before measurements begin at 450 °C. The degassing schedule consisted of extractions at temperatures of 450–1250 °C. The samples were held at the set-point temperatures for a duration of 150 s. The released gas was purified using two SAES getters (one hot and one cold). To determine helium abundances, the sample analyses were bracketed by a calibrated helium spike. Isotope abundances were calculated at the time of admission into the mass spectrometer based upon polynomial regressions fit to the peak hopping scans. All heating steps and spike measurements were corrected for system backgrounds.

2.3. Electron microscopy and spectroscopy

Scanning electron microscopy (SEM) was performed on the as-received nickel particles prior to alumina coating, as well as the coated particles. Energy dispersive X-ray spectroscopy (EDS) was also done on the 25, 50, and 100-cycle ALD samples.

Transmission electron microscopy (TEM) and selective area diffraction (SAD) were performed on the 50-cycle as well as the thermally treated 50-cycle ALD alumina-nickel samples to determine the microstructure and crystal structure of the original and thermally treated samples. Simultaneous scanning TEM (STEM) and electron energy loss spectroscopy (EELS) were used to determine the thickness of the Al_20_3 layers on the 25-cycle, 50-cycle, and 100-cycle ALD alumina-nickel nanoparticles, in addition to the 50-cycle thermally treated (800 C) sample. Bright field TEM images and SAD patterns were acquired on a JEOL 2500SE, while simultaneous STEM images and EELS spectra were acquired on an aberration-corrected JEOL 2100F equipped with a post-column EELS spectrometer. An accelerating voltage of 200 kV was used for the acquisition of (S)TEM images as well as EELS spectra.

2.4. Simulation

We performed molecular modeling on the alumina materials interaction with gases. Interaction between cations and anions in alumina are considered purely ionic except for excluded volume, which is modeled by a short-range Buckingham potential (cutoff distance 10 Å). This leads to the following interaction (eq. (1))

$$E = Ae^{-r/\rho} - \frac{C}{r^6} + \frac{1}{4\pi\varepsilon_0}\frac{q_1 q_2}{r} \quad (1)$$

where A, ρ and C are empirical parameters, r the distance between two ions, q_i the charge of ion i. The long range electrostatic interaction was calculated using Ewald summation. Empirical parameters are found in Ref. [31]. The interaction energy between helium and O^{2-} is described by a 12-6 Lennard Jones potential, with parameters provided in Ref. [32] (cutoff distance 7.5 Å). Helium and Al^{3+} interaction is neglected due to the low polarizability of aluminum compared to oxygen. The construction of simulation models and the simulation of the helium transport property were realized using molecular dynamics (MD) using the LAMMPS suite [33]. Helium retention and absorption was simulated using Grand Canonical Monte Carlo (GCMC) in the Towhee modeling suite [34].

2.4.1. Amorphous alumina and δ-alumina construction

An amorphous alumina model was built using the melt-quench method: starting from the well-relaxed alpha crystal phase (unit cell size: 33.16 × 24.62 × 25.88 Å, 2520 atoms total), the structure was heated from 300 K to 5000 K at a heating rate of 10 K/ps under NPT ($P = 0$) conditions, held at 5000 K for 1 ns and then quenched to the metastable amorphous phase at 300 K at a cooling rate of 10 K/ps. The final structure was equilibrated at 300 K for 3 ns and yields the final density of 3.27 g/cm^3. We refer to this as the "300 K amorphous model" in the following.

δ-alumina is one of the possible intermediate phases in the transformation from amorphous alumina to the final stable α-alumina, and its structure is still actively studied due to its highly defective nature, small crystallite size and coexistence with γ-alumina [35]. Here we chose the δ_1-Al_2O_3 structure, as characterized in Libor et al. [35], as one simulation model to discuss its helium retention behavior. The model (unit cell size: 39.68 × 31.8 × 35.04 Å) has been relaxed and equilibrated under NPT ($T = 300$ K, $P = 0$) conditions for 1 ns (final density 3.75 g/cm^3).

For the following helium retention simulation at temperatures from 300 K to 800 K (in steps of 100 K), the 300 K amorphous model and the δ-alumina model were heated each to the designated temperature with a constant heating rate of 10 K/ps, and equilibrated under NPT ($P = 0$) condition (5 ns for 400 K and 500 K, 8 ns for 600 K and 700 K, and 10 ns for 800 K; lower-temperature structures equilibrate faster since all are heated from original 300 K structure. The higher the temperature, the more the structure is influenced by the heating process, and needs more time to equilibrate.). The generated structures are referred to as the 400 K, 500 K, 600 K, 700 K and 800 K models, respectively.

2.4.2. Helium retention simulation

The quantity of helium retained was first determined at different temperatures using the corresponding models from 300 to 800 K. As we verified in our diffusion simulation, Al^{3+} and O^{2-} ions barely diffuse below 800 K, thus alumina models were kept

rigid in GCMC to reduce computation time, while each model still captures the possible volume expansion at higher temperature conditions. Retention at 100 K was also simulated to ensure a sufficient number of helium atoms were present for transport study. The 300 K model was used for the retention calculation at 100 K. The helium retention isotherm at 300 K was obtained by simulating the retention amount as a function of pressure from 0.1 to 400 MPa.

Three types of Monte Carlo (MC) moves were allowed in the GCMC simulation: insertion, deletion and translation of He atoms. 10^8 total MC steps were performed to reach full equilibration, with insertion acceptance rates from 0.4~0.08% for the amorphous case, depending on temperature. The delta phase has an extremely low acceptance rate, around 10^{-6}.

2.4.3. Helium transport simulation

The motion of helium atoms in amorphous alumina was studied using MD under NPT (P = 1 bar) at temperatures ranging from 300 to 800 K in 100 K steps. The initial configuration and the quantity of absorbed helium atoms come from the GCMC helium retention study at 100 K. Each structure was first heated to the diffusion temperature with a heating rate of 10 K/ps starting from 300 K, and then equilibrated for 10 ns. The diffusion data were collected during a 5 ns production run.

3. Results and discussion

3.1. Helium spectroscopy characterization

After exposure to helium treatment the nickel control samples ("Ni1", "Ni2") as well as the alumina coated nickel samples ("ALD 25", "ALD 50", and "ALD 100") were analyzed for their helium content using mass spectrometric techniques described in the Methods section. The results, normalized by the sample mass, are shown in Table 1. EDS showed more carbon on the 50-cycle ALD samples relative to 25 or 100 cycles, as summarized in Table 1, likely due to process variability in the ALD reactor.

The helium content of the two nickel control samples agrees within 2σ and it is at least an order of magnitude lower than the alumina coated samples. The nickel sample coated with 25 atomic layers of alumina (ALD 25) showed an increased retention of helium approximately 10 times that of the nickel controls, indicating that substantial amounts of helium were retained within the alumina or related structures (see Table 2). Doubling the number of alumina layers to 50 (ALD 50) resulted in the retention of approximately 20 times as much helium. Interestingly, nickel particles coated with 100 atomic layers of alumina showed a 10% decrease in the helium content over those coated with 50 atomic layers. This apparent discrepancy may be due to chemical differences observed in the ALD 100 sample and can be seen from Table 1, where ALD 50 shows higher carbon percentage. For example, the carbon may be more representative of a chemical vapor deposition (CVD) process, where nanoparticles of alumina may have resulted in a porous film instead of a pinhole-free alumina film deposited by ALD. Although the source of these retention differences is not obvious, we observe that the deposition of alumina upon nickel microparticles consistently and substantially increases the retention of helium.

Table 1
Summary of EDS analysis on nickel substrate particles, plus 25, 50 and 100 cycle alumina on nickel particles (normalized to Ni K line amount in Ni substrate sample).

Element/sample	Ni substrate	100 cycle	50 cycle	25 cycle
Ni (K line)	100	26.92	30.31	29.86
O	7.45	9.01	7.41	4.82
C	18.35	8.39	24.64	15.52
Al	3.86	7.39	4.63	2.86
C/Ni(K)	0.18	0.31	0.81	0.52
(Al/2)/(O/3)	0.78	1.23	0.94	0.89

Table 2
Mass normalized (total mass, including both nickel and alumina) helium content for the nickel substrate control samples (Ni1, Ni2) and the alumina coated nickel samples (ALD 25, 50, 100). Errors reported as 1σ.

Sample	^{4}He content (atoms/mg)
Ni1	(1.1 ± 0.1) e10
Ni2	(1.66 ± 0.13) e10
ALD 25	(3.31 ± 0.14)e11
ALD 50	(1.78 ± 0.02)e12
ALD 100	(1.67 ± 0.02)e12

The incremental releases of ^{4}He as a function of temperature from the laser heating experiments are shown in Fig. 1. The data for the nickel control sample indicate that very little helium is released except at the initial heating step and in the final two steps at 1250 and 1430 °C. The elevated helium release at 450 °C likely reflects the loss of loosely bound helium on the surface of the particles. The helium release at high temperatures occurs when the nickel begins to melt (the nickel melting point is 1455 °C). The data for the ALD coated samples show increased helium release as compared to the nickel control, due to the retention of helium within the alumina layers, or at the alumina-nickel interface. All three samples release a majority of the total ^{4}He near the loading temperature of 800 °C. The existence of multiple release peaks suggests there are several ^{4}He binding modes in the structure. High levels of helium release were also observed near the nickel melting temperature for the ALD 25 sample, which suggests that an anomalously high concentration of ^{4}He may have been retained within the nickel substrate, in the absence of an alumina coating. ALD samples not exposed to the helium loading treatment were not analyzed, so the possibility that the ALD process may have contributed to the elevated helium content cannot be discounted. However, the low (177 °C) ALD processing temperature makes this scenario unlikely.

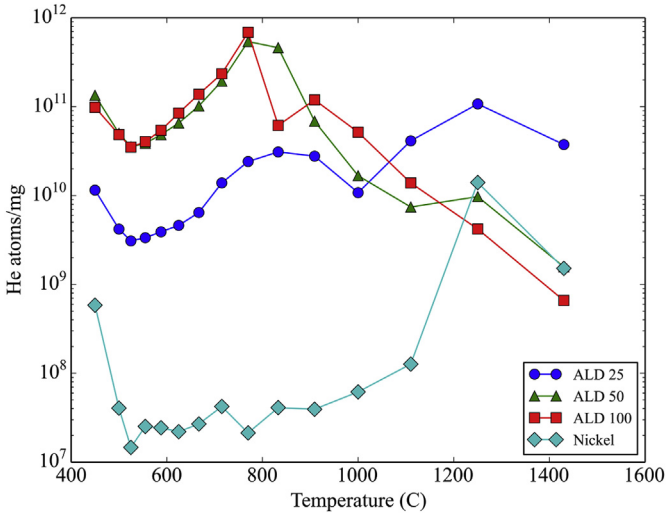

Fig. 1. Helium release data as a function of temperature for the nickel control (cyan diamonds) and the ALD 25, 50 and 100 samples (red circles, blue triangles and purple squares, respectively). (For interpretation of the references to colour in this figure legend, the reader is referred to the web version of this article.)

3.2. Structural analysis of the alumina-Ni particles

The as-received nickel particles are approximately 3 μm in diameter and have significant surface texture as seen in Fig. 2. EELS line scans were acquired across small spikes, which protruded from the larger Ni particles, as shown in the annular dark field (ADF) STEM images in Fig. 3(a), (b), and (c). The integrated intensity of the O K-edge, the Ni $L_{2,3}$ edge, as well as the ADF image intensity were plotted as a function of distance across regions of interest in the individual spikes (Fig. 3 (a), (b), and (c)). EELS provides an approximate oxide thickness from the oxygen content by measuring the distance of the O K-edge intensity, in regions where the Ni $L_{2,3}$ intensity is negligible. This process prevents contribution of an oxygen signal from the nickel oxide layer from being considered in the measurement of the aluminum oxide layer thickness. Furthermore, growth of the native nickel oxide layer is unlikely since the heat of formation for aluminum oxide is much lower than that of nickel oxide. From averaging the oxide thickness for several tip features across several particles for each sample, we obtain an approximate thickness of alumina deposited from the ALD process. The results are summarized in Table 3. The EELS scan details are found in the Supporting Information, Figure S1. The transition between the 25-cycle and 50-cycle deposition is consistent, but the 100-cycle alumina thickness is larger than would be expected based on the 25- and 50-cycle thicknesses. It is also interesting to note that the thickness of the oxide content nearly doubles after 800 °C thermal treatment for 18 h.

The EELS scans performed on the tip features of the alumina-Ni particles reveal that the oxide cutoff is not sharp compared to the nickel profile. This is likely due to three-dimensionality in the tip features and roughness of the nickel surface. In Fig. 3(a) and (b) particularly, the oxide edge appears to overlap with the nickel. This perceived effect is due to the EELS scan detecting both the top and bottom alumina layer, the native nickel oxide layer, with pure nickel in between the top and bottom oxide layers. However, in the center of the tip feature, the oxide signal is significantly reduced due to the increased inelastic scattering probability of the Ni $L_{2,3}$ edge. This is caused by the increase in volume of Ni compared to the alumina and native nickel oxide layers.

3.3. Nanostructure changes due to temperature

After thermally treating the 50-cycle alumina-Ni sample during helium loading, identical STEM and EELS characterization were performed on the samples. The data, summarized in Table 3, indicate that after helium heat treatment the alumina thickness increases. Either oxygen has diffused into the nickel, or else the nickel tip features have receded. From the STEM and EELS analysis shown in Fig. 4, it appears that the thermal treatment resulted in some blunting and void formation in the 50-cycle sample. In Fig. 4(b) particularly, the formation of a void at the tip can be seen in the ADF STEM image in Fig. 4(b), where image intensity approximately scales with the atomic number squared (~Z^2) [36]. The formation of a void is further supported by the corresponding EELS line scan performed vertically down the tip, revealing that some nickel has diffused away from the tip, leaving an alumina-only cage around a void.

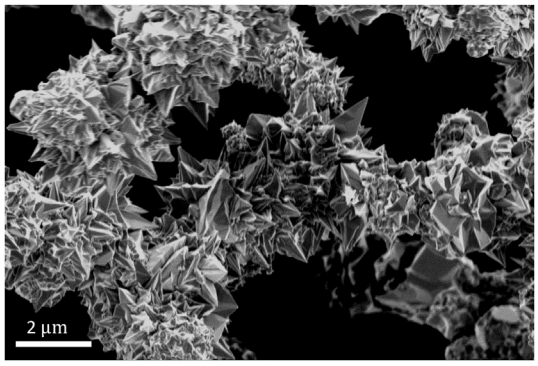

Fig. 2. SEM image of the as-received nickel particles.

TEM bright field images and SAD patterns were also acquired from the 50-cycle (no thermal treatment) and 50-cycle post-thermal treatment samples to characterize the structural changes in the alumina layer after helium loading conditions. From Fig. 5(a) we observe that the 50-cycle pre-heat sample retains an amorphous alumina layer due to the lack of diffraction contrast in the bright field image. This is also supported by the SAD pattern acquired from the same area (Fig. 5(a)), which yields no diffraction spots from an alumina phase. However, after the 800 °C treatment, high resolution TEM (HRTEM) images reveal lattice fringes in the alumina oxide layer (Supporting Information Figure S2). Furthermore, SAD patterns from these samples indicate a transition to a polycrystalline structure, characterized as θ-phase or δ-phase alumina (Fig. 5b ad 5c). This transition is expected, as shown in the literature [37,38]. The amorphous alumina that exists at low temperature immediately after deposition will ultimately transition between several polymorph structures from γ, δ, θ, and ultimately α-phase alumina, or corundum. In particular, both δ and θ-alumina seem to be highly transient states, with the θ to α transformation more widely cited. At temperatures of approximately 1100–1200, the θ to α transformation is observed [39,40], whereas at lower temperatures between 500 and 1000 °C, δ and θ-alumina transformations occur. In terms of structure however, both δ and θ-alumina are highly similar to γ-alumina in density [40].

3.4. Simulated helium retention

For application of alumina to nuclear fuel storage, it is useful to derive the helium retention concentration in the alumina phase (number/volume) from the retention amount normalized by the alumina-Ni sample mass (number/mass) (Table 2). The deposited alumina volume per mass is estimated as alumina film thickness times its specific surface area.

Here we assume Ni particles do not have a significant mass change after alumina deposition. The thickness of the deposited alumina film can be estimated from EELS measurement; however, the difficulty lies in estimating the specific surface area, as the irregular surface of Ni particle can hardly be approximated as spherical (cf. Fig. 2). We therefore employ gas adsorption to estimate the irregular surface area of Ni particles at 0.617 ± 0.014 m^2/g. Note that this is a lower bound for a helium relevant surface, since the measurement was performed with nitrogen. However, with this lower bound the helium retention concentration (number/cm^3) can be calculated as in Table 4.

An alumina simulation model was built to further understand gas retention. Alumina has different polymorphs [41] in the relevant different temperature range (see SAD experiments in Section 3). The amorphous phase is first studied because fluid ALD technique generates this structure, as shown from TEM diffraction measurements (cf. Fig. 5).

Simulated helium's retention concentrations from 300 to 800 K for the amorphous model are shown in Table 5. The retention concentration decreases with temperature. Quantitative analysis reveals the retention concentration is described by the following exponential relation:

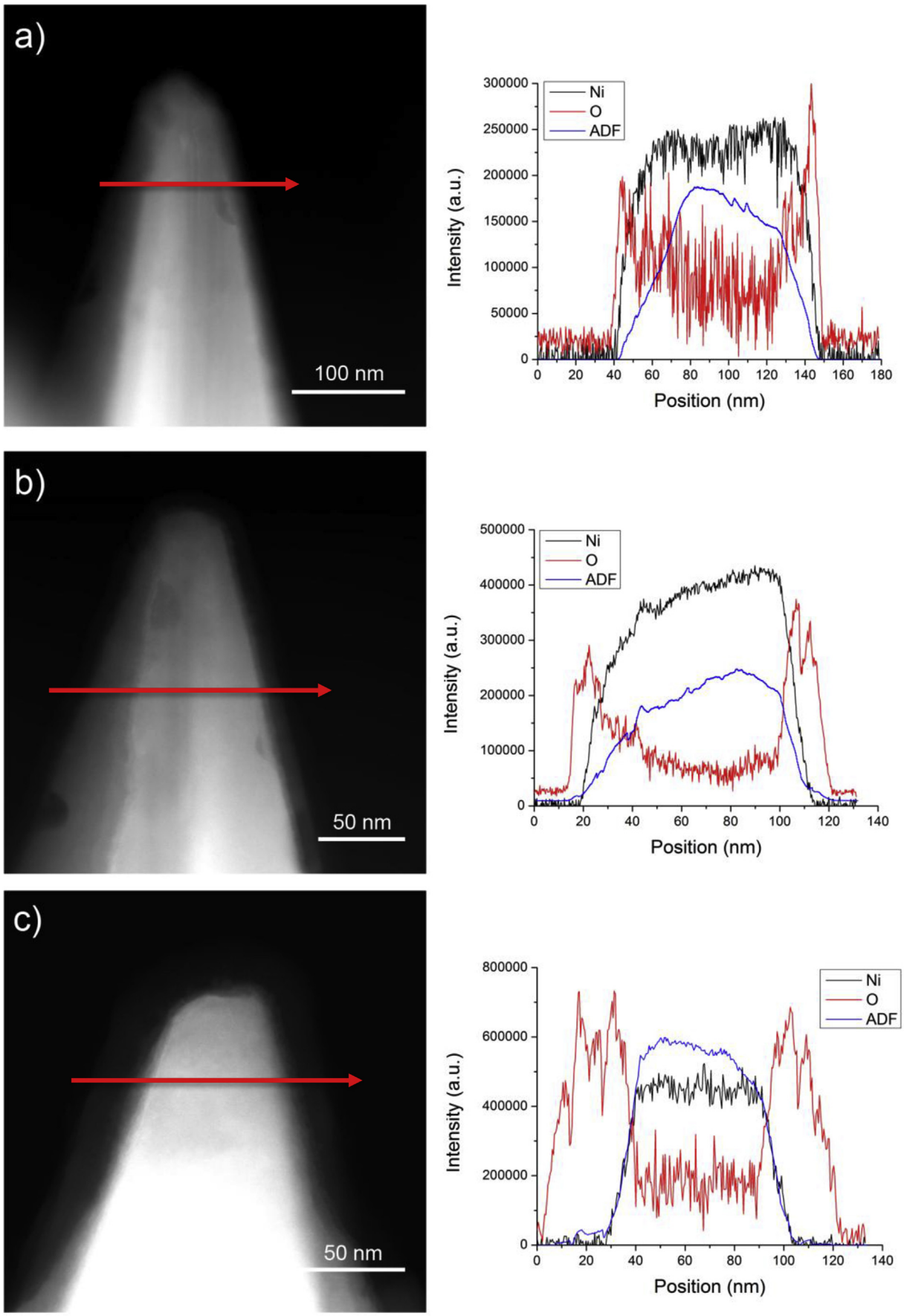

Fig. 3. ADF STEM images and the corresponding EELS data for the (a) 25-cycle, (b) 50-cycle, (c) 100-cycle ALD alumina-coated nickel nanoparticles. The red arrows in the ADF images indicate the region of interest, where the line scans were acquired. The ADF profile in the EELS plots shows the image intensity along the region of interest, and is used a reference. (For interpretation of the references to colour in this figure legend, the reader is referred to the web version of this article.)

Table 3
Average alumina thickness deposited on nickel particles.

	Average alumina thickness (nm)	St. Dev (nm)
25-layer	3.2	0.9
50-layer	5.6	1.4
50-layer (800 °C)	9.5	3.0
100-layer	20.0	4.4

$$C = C_0 e^{\frac{Q}{kT}} \quad (2)$$

where C and C_0 are retention concentrations (number of helium atoms/cm^3), Q is the absorption heat, k the Boltzmann constant and T the temperature.

From plotting ln C versus 1/T (Supporting Information Figure S4), we obtain good linearity indicating consistent absorption heat released in this process, with characteristic energy 0.0999 eV (886 °C).

The fitted value is 2–6 times lower than in the measured case, depending on deposited alumina's thickness. A possible reason for this difference is that the measured specific surface area (made with nitrogen) is a lower bound with respect to helium, therefore the experimental retention concentration calculated here serves as an upper bound. Also, the density of amorphous alumina can vary depending on the cooling rate in experiments. Here only one density is sampled. Lower densities are possible [42], which will increase free volume and thus helium retention. Finally, in addition to absorption in the bulk, adsorption at the surface could occur, leading also to helium retention capacity changes with deposited alumina thickness.

Helium retention in the δ-phase was also simulated. This phase retains very little helium during GCMC in the 300 to 800 K range. This observation may explain, for example, why the initial helium loading temperature at 800 °C is close to the helium release peak from alumina (Fig. 1). The initial loading happens with alumina still

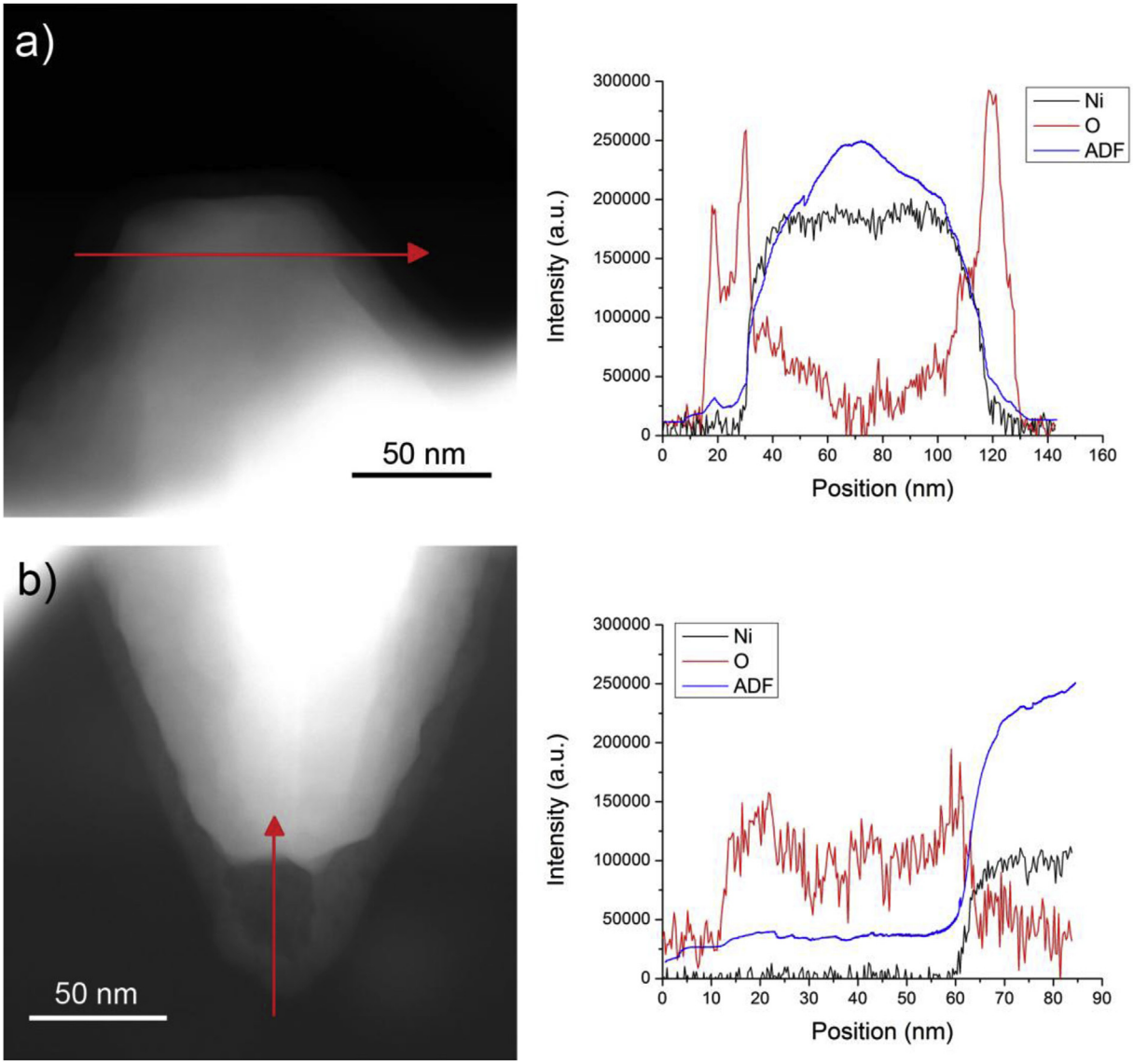

Fig. 4. ADF STEM images and the corresponding EELS line scans for the thermally treated, 50-cycle ALD alumina-coated nickel nanoparticles at (a) normal tip feature and (b) a tip with an unusual void. The red arrows in the ADF images indicate the region of interest, where the line scans were acquired. The ADF profile in the EELS plots shows the image intensity along the region of interest, and is used a reference. (For interpretation of the references to colour in this figure legend, the reader is referred to the web version of this article.)

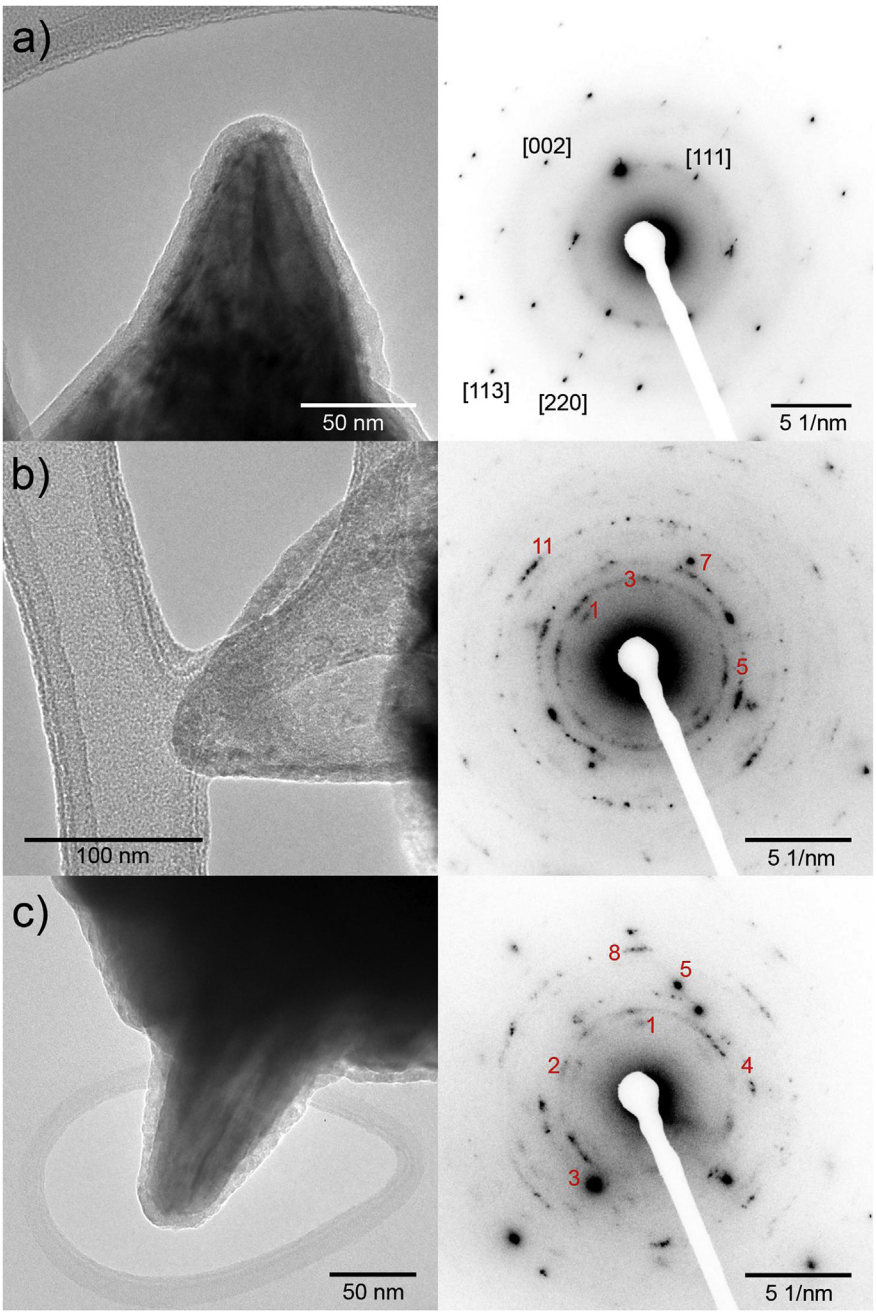

Fig. 5. TEM bright field and SAD patterns acquired from the same regions for the (a) 50-cycle prior thermal annealing, (b) 50-cycle after 800 °C thermal treatment for a hollow tip section, and (c) the 50-cycle after the 800 °C thermal treatment for a solid tip section. The diffraction pattern in b) closely matches that of θ-alumina, while the pattern in c) closely matches that of δ-alumina (see analysis in Supporting Information Tables 1 and 2).

in its amorphous phase, as the transformation to the δ-phase can be slow enough at constant temperature environment to keep some of its amorphous phase to trap helium. However, reheating the sample from 450 to 1430 °C greatly increases the crystallization rate, and helium mobility increases with temperature as well. Both factors lead to rapid liberation of helium from the remaining amorphous phase, since δ-phase alumina has negligible helium solubility. In fact, it is likely that during reheating, 800 °C is a phase transformation point, as a sharp release peak appears at this temperature.

Based on our own TEM results and previous literature [38], the final alumina structure very likely turns completely polycrystalline after enough time of exposure in high temperature. Grain boundaries will thus be present, leading to different retention and transport properties from bulk phase. Our simulation models serve as single crystal structure that do not include grain boundaries, and thus underestimate the retention capacity of polycrystalline materials. In Hurst [26] measurement of helium diffusion in polycrystalline alumina indicates significant helium solubility. Grain boundaries will also facilitate the helium diffusion process, which is important for helium transport as will be discussed in section 3.5.

Pressure is also important to consider for helium retention. van Veen et al. [19] estimated 10^{22} helium cm^{-3} can be generated if the fission product Am is fully decayed, which leads to 40–400 MPa

Table 4
Helium retention concentration (number/cm^3) calculated from experimental data (loading temperature at 800 °C) and simulation results (fitted value at 800 °C). In simulations delta phase alumina showed no retention, but did not account for grain boundaries.

Samples	He#/cm^3	
	Experimental results	Amorphous simulation (fitted value at 800 °C)
25 cycle	2.06×10^{17}	9.6×10^{16}
50 cycle	5.7×10^{17}	
100 cycle	2.7×10^{17}	

Table 5
Simulated helium retention concentration in amorphous alumina structure at different temperatures.

Temperature (K)	Simulated amorphous alumina helium retention (number of He atoms/cm^3)
300	1.51×10^{18}
400	5.7×10^{17}
500	3.6×10^{17}
600	2.4×10^{17}
700	1.8×10^{17}
800	1.2×10^{17}

pressure inside the fuel oxide particle, depending on the porosity of the material. Ferry et al. [2] noted the pressure of a formed gas bubble could be as high as up to 15 GPa. Therefore, the retention capacity of amorphous alumina should also be examined at different pressure conditions. MC reveals that an increase in pressure greatly enhances the retention concentration (Supporting Information Figure S5). Pressure in the GPa range is not considered however, since such high pressures can cause mechanical changes to alumina. At 400 MPa, the retention concentration reaches 3.6×10^{21} helium cm^{-3}. Considering a helium concentration of 4.2×10^{19} cm^{-3} after 300 years in the spent fuel [2], the storage of total helium amount requires the volume ratio between alumina and host fuel material to be around 0.01. For spherical fuel particles with an average fuel particle radius of 3 μm (as noted previously, uranium oxide itself is typically prepared in the form of micron-sized particles), then the required alumina layer thickness is around 10 nm.

3.5. Gas transport properties and simulation results

Transport of helium atoms was simulated in amorphous alumina. The mean square displacement (MSD) of helium was characterized at temperatures from 300 to 800 K. Below 800 K, helium atoms can be easily trapped in local potential wells, reflected by the fluctuations in the MSD (see, for example, Supporting Information Figure S6). The sudden fluctuations correspond to the jump of He atoms from one local minimum position to another. At 800 K, regular diffusion becomes noticeable and a diffusion coefficient D can be obtained by linear fitting according to eq. (3):

$$D = \frac{r^2}{6t} \tag{3}$$

where r^2 is the mean square displacement and t is time. Amorphous alumina yields D at 800 K to be 4.5×10^{-12} m^2/s. A direct comparison with experimental diffusion values in our own system is not possible, since the kinetic analysis based on helium release (Fig. 1) reveals that diffusion is unlikely to be the rate limiting step for helium release measured by spectroscopy (Table S3). Instead, we are likely measuring thermally-activated desorption from the internal nickel-alumina surface [43], since little helium release is measured in the nickel control particles. Nevertheless, diffusion is still the main transport mechanism over micrometer ranges or larger as within fuel pellet, and therefore merits further examination. In experiments the presence of voids and grain boundaries further facilitate diffusion in ways not captured by this simplified model. However, our model can be used as a lower bound estimation for diffusion within amorphous alumina.

A model developed by Turnbull and Friskney (eq. (4)) can be employed to estimate the effect of a second, higher-diffusivity phase in the nuclear fuel. This model, optimized for the diffusion of fission products which inherently have a decay time constant, is effective in showing an approximation of how the physical dimensions of the system affect the fractional release of generated byproducts, such as helium, from grain boundaries. The model is applicable to different gases, including helium, as the diffusion parameters can vary correspondingly to the specific type of gas examined. We assume that the alumina-coated nickel nanoparticle system behaves similarly to the large-grained (3–5 μm diameter) uranium oxide system for which the equation was developed, except the diffusion coefficient of helium in uranium oxide is slower than in in nickel case. The pre-exponential factor and activation energy in uranium oxide are at the order of 10^{-10} m^2/s and around 2 eV [27], respectively, while that in nickel are around 10^{-6} m^2/s and 0.81 eV [44]. This leads to a smaller D_L value with real fuel materials in eq. (4). Instead of having a fixed physical system as done by Turnbull and Friskney, however, here the radius of fuel pellet was varied from 1 mm to 100 mm. In reality the radii of typical fuel pellets are on the order of 10 mm [45]. Because the model does not include a packing factor or take porosity into consideration, the individual pellet size can be treated as the total system size when the fuel rod is comprised of multiple pellets compacted homogeneously. Values of the radioactive decay constant λ were varied from 10^{-7} to 10^{-1} s^{-1} in Turnbull and Friskney. Other constants are shown below.

$$F_{gb} = \frac{9\delta A}{2a\lambda R}\sqrt{\frac{D_{gb}}{(A+\lambda)}} * \left[\coth\left(R\sqrt{\frac{(A+\lambda)}{D_{gb}}}\right) - \left(\frac{1}{R}\sqrt{\frac{D_{gb}}{(A+\lambda)}}\right)\right] \tag{4}$$

for

F_{gb} = fractional release of fission products
δ = grain boundary thickness, (10 nm)
a = grain radius (3 μm)
R = radius of fuel pellet material

D_{gb} = diffusion coefficient through grain boundary material (3.6×10^{-11} m^2/s, average diffusion coefficient of several polycrystalline alumina samples from reference at 973 K [26])
D_L = diffusion coefficient through bulk grain material (5×10^{-18} m^2/s for nickel case, upper bound estimation at 973 K [46,47])
λ = characteristic decay time constant

$$A = 2\sqrt{\frac{(D_L\lambda)}{\delta}}$$

The predicted release fraction as a function of pellet size is shown in Fig. 6. The inclusion of alumina, which has a diffusion constant about 7 magnitudes of order greater than nickel [26], improves the fractional release of fission products by 3 orders of magnitude. For the case of uranium oxide, such improvement is expected be more significant as the D_L is even smaller.

Fig. 6 shows that the presence of a secondary material with a higher diffusion coefficient can improve the transport properties of the system substantially, for a large range of pellet sizes. Such improvement becomes more significant with increasing temperature, for example if the diffusion coefficient is about a hundred times higher at higher temperature, the release fraction will be improved by approximately one order of magnitude with the same pellet size. From Equation (4), the secondary material's diffusion coefficient (D_{gb}) is approximately proportional to the fractional release (F_{gb}). However, variations in the physical properties such as the nickel particle size, helium generation time and overall pellet size have greater consequences on the fractional release. From Fig. 6, the decrease of pellet size by 2 orders of magnitude leads to the increase of fractional release at the same order. The effect of helium generation rate, as reflected by λ, is shown in Fig. 7.

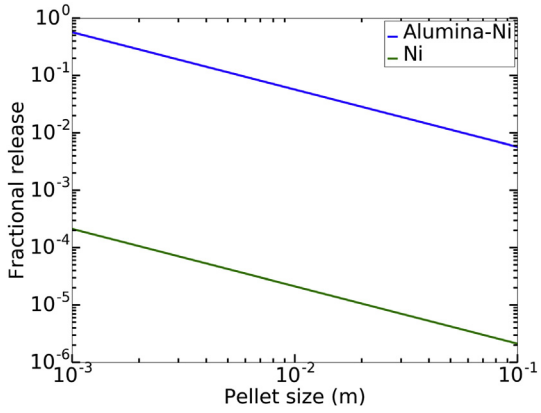

Fig. 6. Application of the Turnbull Equation to observe the effect of overall pellet size to the fractional release of helium between the alumina-Ni and Ni systems at room temperature with $\lambda = 5 \times 10^{-6}$ s^{-1}).

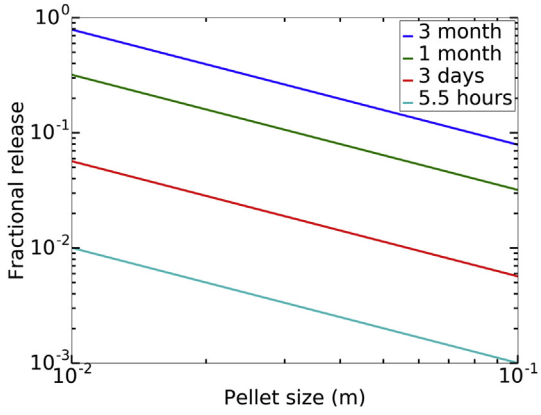

Fig. 7. Fractional release assuming different helium generation times.

The different time scales in Fig. 7 represent $1/\lambda$, where λ is the radioactive decay rate that was varied from 10^{-7} to 10^{-1} s^{-1} in Turnbull and Friskney. The longer the decay time, the slower the helium will be generated. With a time scale increasing from hours (6 h correspond to $\lambda \sim 10^{-4}$ s^{-1}) to months (3 months correspond to $\lambda \sim 10^{-7}$ s^{-1}), the fractional release is improved by 2 orders of magnitude. This behavior is due to the fact that the fractional release depends on the ratio between the release rate (diffusion rate) and the generation rate of helium. Fig. 7 shows that an 80% fractional release or higher can be achieved with a realistic 10 mm diameter pellet, assuming a radioactive decay time of 3 months or longer.

4. Conclusions

Our results illustrate the potential for thin layers of helium-retaining materials to act as retention reservoirs and diffusion paths in spent nuclear fuel. In this work alumina layers were formed on surrogate nickel particles by atomic layer deposition. Alumina thicknesses ranged from 3 nm to 20 nm, as confirmed by EELS. Helium was loaded into the particles at 800 °C for over 18 h in a tube furnace. From TEM and SAD characterization, the originally-deposited alumina was amorphous, and experienced a phase transition to θ-alumina and/or δ-alumina at a temperature equal or lower than 800 °C, consistent with the observations by others [38] on heated ALD alumina films.

Helium spectroscopy measurements indicate that the thin alumina layer can increase the helium storage capacity up to two orders of magnitude relative to the uncoated nickel. Monte Carlo simulations suggest that such improvement could be realized by an amorphous alumina phase, where at 400 MPa its retention capacity at 300 K can fully contain the produced helium in spent fuel. In the model, helium retention decreases rapidly as the alumina is crystallized; however, the model does not reflect the critical role of grain boundaries for helium transport and storage. From literature values of helium diffusion rates in polycrystalline alumina [26], we anticipate that helium transport out of macroscopic fuel pellets through a geometrically-connected alumina phase may be feasible for long-term spent fuel storage.

This work motivates the future investigation of higher-temperature materials, such as yttria-stabilized zirconium, which may also be formed on nuclear fuel particles by ALD. Our work with particle ALD-coated alumina shows a potential path for volumetrically incorporating a very low volume phase of this material into the fuel pellet, while maintaining a uniform spatial distribution to facilitate both retention and transport.

Acknowledgments

Authors gratefully acknowledge the assistance of Dr. Harold Levie (LLNL) for sample preparation and helpful comments during manuscript preparation. We also acknowledge LLNL's Fowzia Zaka for SEM and EDS measurements. This research was partially supported by the U. S. Department of Energy, Office of Nuclear Energy, Nuclear Energy University Program under Grant No. DE–NE0000704. Parts of this work were performed under the auspices of the U.S. Department of Energy by Lawrence Livermore National Laboratory under Contract DE-AC52-07NA27344.

Appendix A. Supplementary data

Supplementary data related to this article can be found at https://doi.org/10.1016/j.jnucmat.2017.11.029.

References

[1] F. Rufeh, D.R. Olander, T.H. Pigford, Nucl. Sci. Eng. 23 (1965) 335.
[2] C. Ferry, J.-P. Piron, A. Ambard, J. Nucl. Mater 407 (2010) 100.
[3] C. Ferry, C. Poinssot, P. Lovera, A. Poulesquen, V. Broudic, C. Cappelaere, L. Desgranges, P. Garcia, C. Jegou, D. Roudil, CEA Saclay, 2005.
[4] C. Ferry, C. Poinssot, C. Cappelaere, L. Desgranges, C. Jegou, F. Miserque, J.P. Piron, D. Roudil, J.M. Gras, J. Nucl. Mater 352 (2006) 246.
[5] C. Ronchi, J.P. Hiernaut, J. Nucl. Mater 325 (2004) 1.
[6] Z. Talip, T. Wiss, V. Di Marcello, A. Janssen, J.-Y. Colle, P. Van Uffelen, P. Raison, R. Konings, J. Nucl. Mater 445 (2014) 117.
[7] T. Wiss, J.-P. Hiernaut, D. Roudil, J.-Y. Colle, E. Maugeri, Z. Talip, A. Janssen, V. Rondinella, R.J.M. Konings, H.-J. Matzke, W.J. Weber, J. Nucl. Mater 451 (2014) 198.
[8] D.H.W.P. Carbol, T. Wiss, P. Fors, Compr. Nucl. Mater. 5 (2012) 389.
[9] K. Une, I. Tanabe, M. Oguma, J. Nucl. Mater 150 (1987) 93.
[10] S. Kashibe, K. Une, J. Nucl. Mater 254 (1998) 234.
[11] J.A. Turnbull, C.A. Friskney, J. Nucl. Mater 58 (1975) 31.
[12] D.M. King, X. Liang, A.W. Weimer, Powder Technol. 221 (2012) 13.
[13] H.W.R. De, Y. Nivas, General Electric Company, US3872022 A, 1975.
[14] K.W. Lay, H.S. Rosenbaum, J.H. Davies, General Electric Company, US4869867, 1989.
[15] K.W. Lay, H.S. Rosenbaum, J.H. Davies, M.O. Marlowe, General Electric Company, US4869866, 1989.
[16] M.O. Marlowe, General Electric Company, US5946364, 1999.
[17] M.O. Marlowe, General Electric Company, US6190582, 2001.
[18] M. Streit, F. Ingold, J. Eur. Ceram. Soc. 25 (2005) 2687.
[19] A. van Veen, R.J.M. Konings, A.V. Fedorov, J. Nucl. Mater 320 (2003) 77.
[20] R.L. Puurunen, J. Appl. Phys. 97 (2005) 121301.
[21] C.W. Bale, E. Bélisle, P. Chartrand, S.A. Decterov, G. Eriksson, A.E. Gheribi, K. Hack, I.H. Jung, Y.B. Kang, J. Melançon, A.D. Pelton, S. Petersen, C. Robelin, J. Sangster, P. Spencer, M.A. Van Ende, Calphad 54 (2016) 35.
[22] W.A. Lambertson, M.H. Mueller, J. Am. Ceram. Soc. 36 (1953) 329.
[23] G.S. Mani, G.J. McCallum, A.T.G. Ferguson, Nucl. Phys. 19 (1960) 535.
[24] M.D. Kaminski, M.M. Goldberg, J. Nucl. Mater 304 (2002) 182.
[25] T. Ishizu, T. Yokoyama, H. Endo, M. Tokiwai, H. Ninokata, J. Nucl. Sci. Technol. 47 (2010) 684.
[26] J.J. Hurst, Helium Diffusion Rate, Permeation Rate, and Activation Energy for Polycrystalline Alumina, 1961.
[27] K. Nakajima, H. Serizawa, N. Shirasu, Y. Haga, Y. Arai, J. Nucl. Mater 419 (2011) 272.
[28] D.M. King, J.A. Spencer Ii, X. Liang, L.F. Hakim, A.W. Weimer, Surf. Coat. Technol. 201 (2007) 9163.
[29] J.D. Ferguson, A.W. Weimer, S.M. George, Thin Solid Films 371 (2000) 95.
[30] J.R. Wank, S.M. George, A.W. Weimer, J. Am. Ceram. Soc. 87 (2004) 762.
[31] G. Gutiérrez, A.B. Belonoshko, R. Ahuja, B. Johansson, Phys. Rev. E 61 (2000) 2723.
[32] P.I. Pohl, Mol. Phys. 89 (1996) 1725.
[33] S. Plimpton, J. Comput. Phys. 117 (1995) 1.
[34] M.G. Martin, Mol. Simul. 39 (2013) 1212.
[35] L. Kovarik, M. Bowden, A. Genc, J. Szanyi, C.H.F. Peden, J.H. Kwak, J. Phys. Chem. C 118 (2014) 18051.
[36] P. Hartel, H. Rose, C. Dinges, Ultramicroscopy 63 (1996) 93.
[37] M.A. Trunov, M. Schoenitz, E.L. Dreizin, Combust. Theor. Model 10 (2006) 603.
[38] X. Liang, N.-H. Li, A.W. Weimer, Microporous Mesoporous Mater 149 (2012) 106.
[39] H. Schaper, L.L. Van Reijen, Thermochim. Acta 77 (1984) 383.
[40] H.-L. Wen, F.-S. Yen, J. Cryst. Growth 208 (2000) 696.
[41] Y. Wang, C. Suryanarayana, L. An, J. Am. Ceram. Soc. 88 (2005) 780.
[42] P. Vashishta, R.K. Kalia, A. Nakano, J.P. Rino, J. Appl. Phys. 103 (2008) 083504.
[43] D. Edwards, E.V. Kornelsen, Surf. Sci. 44 (1974) 1.
[44] V. Philipps, K. Sonnenberg, J.M. Williams, J. Nucl. Mater 107 (1982) 271.
[45] D.G. Cacuci, Handbook of Nuclear Engineering, Springer Science & Business Media, 2010.
[46] M.B. Lewis, K. Farrell, Nucl. Instrum. Methods Phys. Res. B 16 (1986) 163.
[47] A.J. Adams, W.G. Wolfer, J. Nucl. Mater 158 (1988) 25.